Plasma Physics and
Controlled Fusion

PAPER • OPEN ACCESS

Characterization of a microwave reflectometer for edge density profile measurements at the ICRH antenna on Wendelstein 7-X

To cite this article: D López-Rodrıguez *et al* 2026 *Plasma Phys. Control. Fusion* **68** 075022

IOP Publishing Plasma Phys. Control. Fusion 68 (2026) 075022 https://doi.org/10.1088/1361-6587/ae871f

Plasma Physics and Controlled Fusion

PAPER

Characterization of a microwave reflectometer for edge density profile measurements at the ICRH antenna on Wendelstein 7-X

Check for updates

OPEN ACCESS

RECEIVED
29 January 2026

REVISED
3 April 2026

ACCEPTED FOR PUBLICATION
7 July 2026

PUBLISHED
17 July 2026

D López-Rodrıguez[1,2,*], A Krämer-Flecken[3], H M Xiang[4], X Han[5], K Crombé[1,2], J Ongena[1], D A Castaño-Bardawil[1], B Schweer[1], A Adriaens[1,2], M Verstraeten[1], M Vervier[1], P Dumortier[1], G C Amanekwe[1], T Schröder[6], P Kallmeyer[6], M Stern[6], D Hartmann[6], M Vergote[1]
and the W7-X team

[1] Laboratory for Plasma Physics, LPP-ERM/KMS, Brussels, Belgium
[2] Department of Applied Physics, Ghent University, Ghent, Belgium
[3] Institute of Fusion Energy and Nuclear Waste Management, Forschungszentrum Jülich GmbH, Jülich, Germany
[4] Shenzhen Institute of Research and Innovation, University of Hong Kong, Shenzhen, People's Republic of China
[5] University of Wisconsin-Madison, Madison, United States of America
[6] Max-Planck Institute for Plasma Physics, Greifswald, Germany
[7] See O. Grulke *et al* 2024 (https://doi.org/10.1088/1741-4326/ad2f4d) the W7-X team.
[*] Author to whom any correspondence should be addressed.

E-mail: luisdaniel.lopezrodriguez@ugent.be

Keywords: stellarator, reflectometer, density profile, ion cyclotron resonance heating

Abstract

A microwave reflectometer has been integrated into the ion cyclotron resonance heating (ICRH) antenna system of the Wendelstein 7–X (W7-X) stellarator to measure electron density profiles in the edge region of the plasma. The diagnostic operates in X-mode and is specifically designed to probe the plasma directly in front of the ICRH antenna, where local density conditions critically influence radio-frequency power coupling. Dedicated calibration procedures were developed to improve the data collection and analysis. Electron density profiles, reconstructed from the corrected beat frequencies, show good agreement with measurements from Thomson scattering and Alkali beam emission spectroscopy, validating the reflectometry measurement. The edge density profiles can be measured when ICRH power is injected and exhibit the expected response to global density ramp-up experiments. These results demonstrate the capability of the microwave reflectometer to provide reliable edge density measurements and establish a basis for future studies of ICRH plasmas in W7-X.

1. Introduction

The stellarator concept offers clear advantages for magnetic confinement fusion, principally steady-state operation and the absence of current-driven disruptions. Wendelstein 7-X (W7-X), the largest HELIAS type stellarator [1] currently in operation, has been designed and optimized to minimize neoclassical transport and to demonstrate high-performance plasma operation [2]. Recent experimental campaigns have demonstrated the stellarator's capability for long-pulse operation and developed advanced heating and confinement scenarios [3].

A central scientific objective of W7-X is the experimental validation of fast particles confinement under reactor-relevant conditions, which is essential for efficient plasma heating and the viability of stellarators as fusion power plants [4]. Neutral beams can be used to explore the predicted improvement of fast ion confinement at higher plasma beta [5]. Another way to study this effect is to use an ion cyclotron resonance heating (ICRH) system. For this reason, an ICRH antenna has been developed, commissioned, and installed on W7-X [6]. The two-strap ICRH antenna operates in a frequency range of 25 MHz to 38 MHz, with a pulse length of up to 10 seconds, and can deliver radio-frequency (RF) power levels up to 1.5 MW. Its primary purpose is the generation of fast ions in W7-X, and an operational scheme to generate trapped fast ions with the ICRH system has been explored using numerical tools [7]. In addition, the ICRH system provides capabilities for ion cyclotron wall conditioning, target plasma generation, and auxiliary plasma heating in future experimental campaigns.

Experiments and simulations have shown that the efficiency of RF power coupling from the ICRH antenna to the plasma is strongly influenced by the electron density profile in the scrape-off layer (SOL) in front of the antenna [8]. The local edge density affects wave propagation and absorption, antenna loading, and matching conditions, making accurate density profile measurements a key requirement for understanding and optimizing ICRH performance. In W7-X, variations of the edge density profiles can impact the interaction between the antenna and the plasma, reinforcing the need for a localized and reliable diagnostic close to the antenna.

Microwave reflectometry provides a non-invasive diagnostic approach for measuring electron density profiles in magnetically confined plasmas and has been successfully applied in a wide range of fusion devices like tokamaks [9–12] and stellarators [13–15]. On W7-X, a reflectometer has been integrated into the ICRH antenna module to enable direct measurements of the edge electron density in front of the antenna during ICRH operation [16, 17]. Reflectometry has also been used to estimate edge density profiles in front of heating systems in other machines [18, 19]. These measurements are essential for characterizing the plasma conditions relevant to wave coupling and for supporting the interpretation of ICRH experiments.

The paper is structured as follows; section 2 provides a detailed description of the W7-X density profile reflectometry system. Section 3 shows the challenges faced in the use of the diagnostic and how to improve and interpret the acquired data. In section 4, the results obtained during the experiments of the operational phase OP2.3 are shown, focusing on comparing the estimated density profiles with other diagnostics available in the stellarator. Finally, section 5 gives concluding remarks and perspectives for future work.

2. Description of the density profile microwave reflectometer

A microwave reflectometer has been designed and installed in the ICRH antenna system of the W7-X stellarator for measurements of the electron density profiles in the plasma edge region in front of the antenna. An extensive description of the design of the diagnostic can be found in [16, 17, 20].

The reflectometer utilizes a frequency modulated continuous wave (FMCW) scheme with a heterodyne detection method. To be able to measure the density in front of the ICRH antenna with sufficient radial resolution, the diagnostic is polarized in extraordinary mode (X-mode). The X-mode upper cutoff frequency is given by:

$$\omega_{\mathrm{X,upper}} = \frac{1}{2}\left(\omega_{\mathrm{ce}} + \sqrt{\omega_{\mathrm{ce}}^2 + 4\omega_{\mathrm{pe}}^2}\right) \tag{1}$$

where the electron cyclotron frequency is $\omega_{\mathrm{ce}} = |e|B/m_{\mathrm{e}}$ and the plasma frequency is $\omega_{\mathrm{pe}} = \sqrt{e^2 n_{\mathrm{e}}/\varepsilon_0 m_{\mathrm{e}}}$. Here, B denotes the strength of the magnetic field at this location, n_{e} the electron density, e the elementary charge, m_{e} the electron mass, and ε_0 the vacuum permittivity [21]. As shown in equation (1), the operation in X-mode has cutoffs that depend on both electron density and magnetic field, so it provides access to a wide range of electron densities when the probing frequency is changed and gives a more reliable mapping of the profiles, making it well suited for edge density measurements in W7-X.

Figure 1(c) shows a 3D model of the electronics box of the reflectometer (in orange), the waveguides inside the movable ICRH antenna system, and the sectoral horn antennas (in blue) located between the straps of the ICRH antenna. Figure 1(a) shows one pair of bistatic horn antennas used to launch and receive the microwaves at a sweeping frequency. The diagnostic has been designed to operate in close proximity to the ICRH antenna straps [16, 17]. The position of the reflectometer enables localized probing of the plasma directly in front of the antenna, providing electron density profile measurements that are in the RF coupling region.

The reflectometer system has two frequency bands: E-band (60–90 GHz) and W-band (75–110 GHz), which correspond to cutoff electron densities up to approximately $n_{\mathrm{e}} \leqslant 6.0 \times 10^{19}\,\mathrm{m}^{-3}$ at the nominal central magnetic field of $B_0 = 2.5$ T. The frequency bands were selected to cover the plasma edge region in front of the ICRH antenna [16].

The 3D model in figure 1(c) shows two transmission lines, each equipped with bistatic sectoral horn antennas. The bottom line is used for E-band and the top one for W-band. The reflectometer can generate density profiles with a radial resolution of approximately 0.01 m and operates with a timing of 40 µs per frequency sweep.

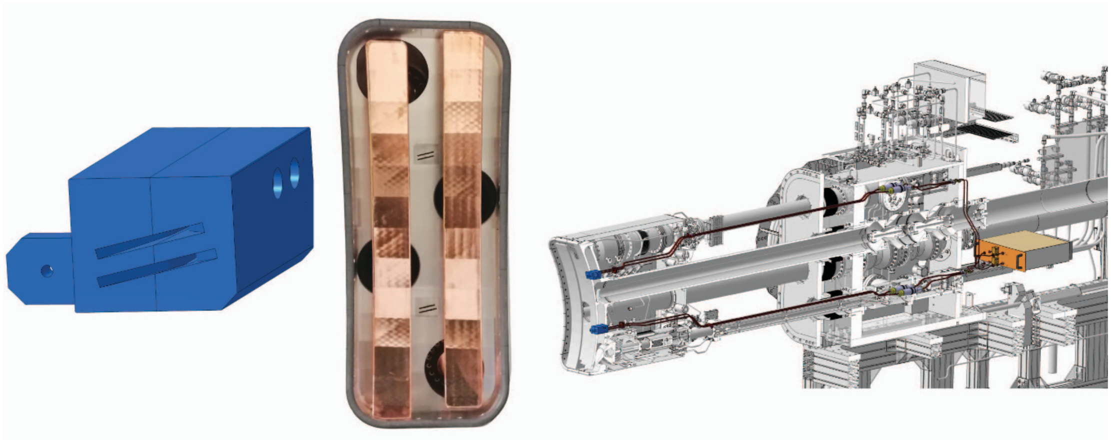

(a) (b) (c)

Figure 1. (a) Bistatic sectoral horn antenna used to launch and receive the microwaves. (b) Front view of the ICRH antenna and the microwave reflectometer sectoral horn antennas between the copper straps. (c) 3D model of the microwave reflectometer inside the ICRH antenna system in W7-X. Highlighted in color are the electronics box on the right (in orange), the top and bottom waveguides used for W- and E-band respectively, and the sectoral horn bistatic antennas (in blue).

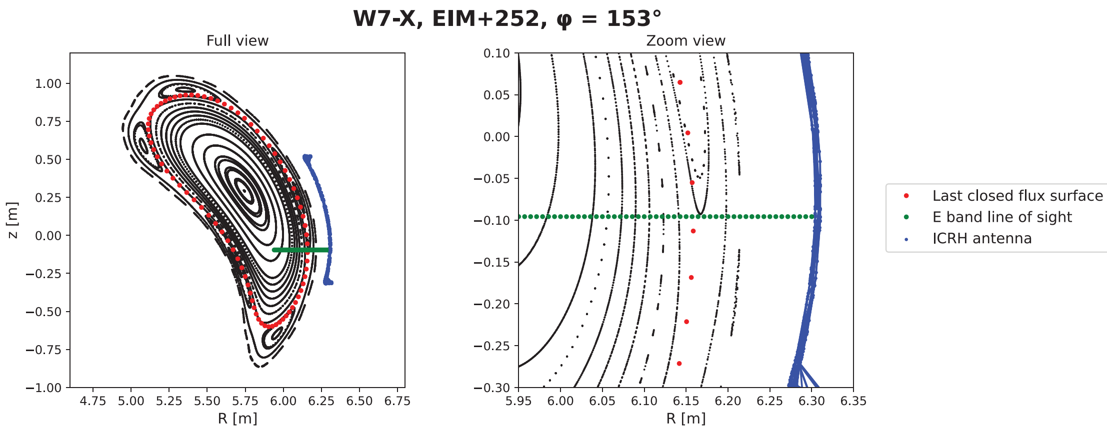

Figure 2. Poincaré map calculated for the standard magnetic field configuration at the toroidal position in front of the ICRH antenna in W7-X. The last closed flux surface is plotted in red, the contour of the ICRH antenna in blue, and the line of sight of the E-band sectoral horn antenna in green. The panel on the left shows the full view of the plasma shape and the panel on the right zooms in the region of interest to highlight the intersection of the line of sight of the reflectometer with the 5/5 island chain.

One of the unique characteristics of this diagnostic is that the sectoral horn antennas of the microwave reflectometer are located inside the metallic housing of the ICRH antenna, approximately 117 mm behind the copper straps. Figure 1(b) presents a front view of the W7-X antenna system, the small slits between the ICRH antenna straps are the top and bottom bistatic horn antennas, custom made for this diagnostic, used for W-band and E-band respectively. The system has been designed to prevent the reflection from the straps by modifying the shape of the horn antennas, presented in figure 1(a), to minimize the side lobes of the beam [20].

Figure 2 presents the Poincaré map at the toroidal position in front of the ICRH antenna in the stellarator. The flux surfaces have been calculated with the widely used variational moment equilibrium code (VMEC) [22] and read from the W7-X database for the standard magnetic field configuration [23]. The last closed flux surface (LCFS) is highlighted in the plot, this can be defined as the last field line that traces out a closed 2D line in the Poincaré map, with lines that do not intercept any components [24]. The shape of the ICRH antenna has been designed to follow the shape of the LCFS in the standard field configuration to improve the coupling efficiency of the heating system [25].

Figure 2 also shows the line of sight (LOS) of the bottom sectoral horn antenna of the reflectometer. The bottom waveguide was used for the microwave frequencies in the E-band. The top waveguide shown in figure 1(c) was reserved to the W-band frequencies, but the data could not be used during the last operational phases due to technical problems. For this reason, the density profiles presented in this

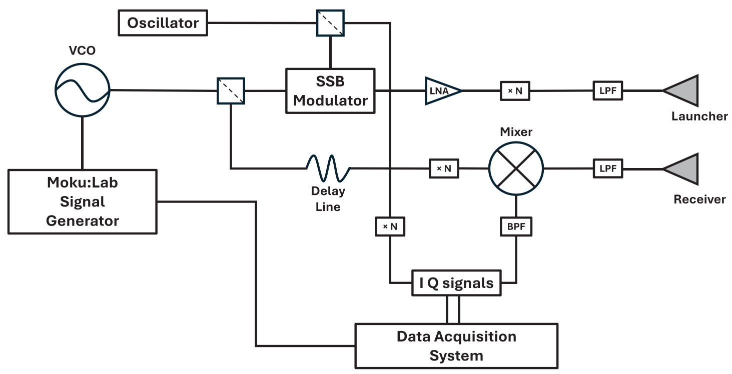

Figure 3. Electronics scheme of the microwave reflectometer. The simplified scheme shows a representation of the connections between the elements in the reflectometer box, including the use of low noise amplifiers and filters to improve the collected signals.

paper have been calculated using the E-band only. The LOS is defined perpendicular to the closed flux surfaces of the plasma in the standard magnetic field configuration and it was designed to pass close to the X-point of the magnetic field island in the SOL in this configuration [16]. The right hand side panel of figure 2 shows a zoom view in the edge region to highlight the intersection LOS of the microwave reflectometer with the 5/5 island chain.

A scheme of the electronic box for one frequency band is presented in figure 3. It uses a proven design that has been operated in other reflectometer systems in magnetic confinement fusion devices [26, 27]. The microwave signal is generated by a voltage-controlled oscillator (VCO), two of these are used to generate the signal for the E- and W-band branches, individually. The waveform given as an input to the VCO can be remotely controlled via a programmable waveform generator and should be calibrated to provide a linear frequency sweep. The output signal from the VCO is coupled with a signal of the quartz oscillator in the single side-band modulator to realize a heterodyne detection. The electronic scheme provides the in-phase (I) and quadrature (Q) signals, which allow the detection of the absolute phase and amplitude that is required for the profile inversion process [16].

3. Challenges in signal processing

Once the I and Q components of the reflected signal corresponding to a frequency sweep are acquired, a sliding fast Fourier transform (FFT) is applied to the data. This approach provides a time-resolved representation of the spectral content of the signal by computing the frequency spectrum for each subsequent sliding time window. The temporal evolution of the signal is visualized in the form of a spectrogram, which is a powerful tool for identifying and suppressing unwanted frequency components. From the spectrogram, the beat frequency can be extracted by tracking the maxima of the spectral amplitude.

The beat frequency describes the temporal phase variation, expressed as $\mathrm{d}\phi/\mathrm{d}t$, and is directly related to the group delay τ_g of the probing wave. This group delay corresponds to the propagation time within the diagnostic system, including the delay introduced by the transmission lines and the round-trip propagation time between the antenna and the cutoff layer. For a linear frequency sweep, this relation can be expressed as:

$$f_\mathrm{beat} = \frac{\mathrm{d}\phi}{\mathrm{d}t} = \frac{1}{2\pi}\frac{\mathrm{d}\phi}{\mathrm{d}f}\frac{\mathrm{d}f}{\mathrm{d}t} = \tau_\mathrm{g}\frac{\mathrm{d}f}{\mathrm{d}t} \tag{2}$$

where $\mathrm{d}f/\mathrm{d}t$ is the microwave frequency sweep rate defined by the electronics. The group delay is then converted into a radial position through the integration of the inverse group velocity along the propagation path.

3.1. Calibration of the electronics

The microwave reflectometer operates using a FMCW scheme. A key requirement for accurate FMCW reflectometry is a linear relationship between the instantaneous microwave frequency and time during the frequency sweep. As can be observed in equation (2), deviations from a constant $\mathrm{d}f/\mathrm{d}t$ directly affect the proportionality between the beat frequency and the propagation group delay, introducing systematic distortions in the reconstructed density profile.

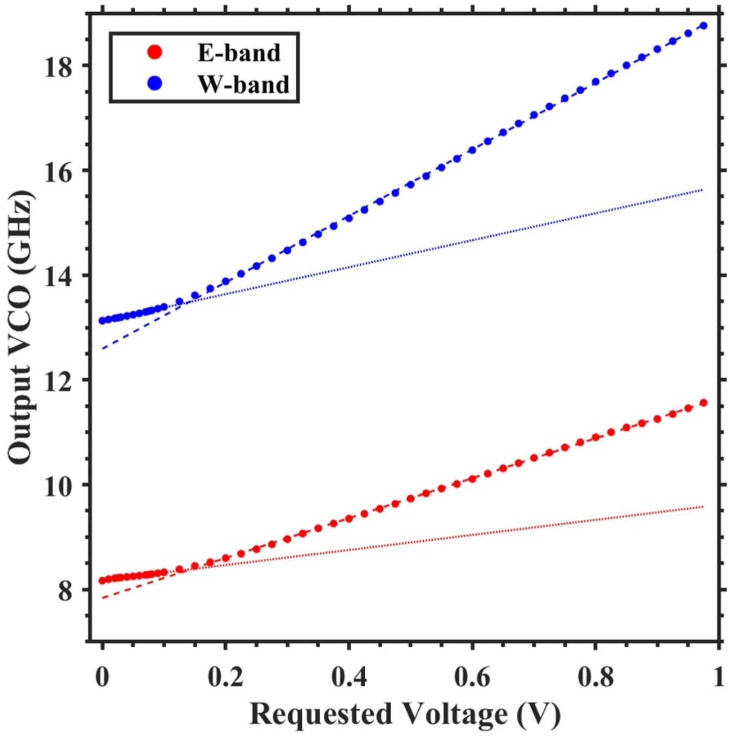

Figure 4. Output of the voltage controlled oscillator as a function of the requested voltage on the arbitrary waveform generator for both frequency bands. The plots show a nonlinear relation between the output of the VCO frequency and the applied voltage. Two linear fits are shown to highlight the nonlinearity of the measured frequency response.

Figure 4 shows the experimental output frequency of the VCO as a function of the applied control voltage for both E- and W-band, measured by a spectrum analyzer. It can be observed that the output frequency of the VCO exhibits an intrinsic nonlinear dependence on the applied waveform voltage. The experimental data shows that the output of the VCO is piecewise linear but globally nonlinear. Two linear fits are shown to highlight the nonlinearity of the measured frequency response.

If a simple linear voltage ramp is applied with the arbitrary waveform generator, this nonlinear VCO response results in a nonlinear frequency sweep. As a consequence, even for a fixed reflection point, such as a metallic mirror placed at a constant distance from the antenna, the measured beat frequency is no longer constant in time but shows significant variations over the sweep. This effect can be seen on the top part of figure 5, where a linear requested voltage produces a non-constant beat frequency, especially at the beginning of the frequency sweep, where the VCO output varies the most.

To correct for this issue, the frequency response of the VCO was characterized prior to plasma operation in the laboratory. Based on the measured response, a calibrated voltage waveform was constructed such that the resulting output frequency varies as linearly as possible with time. This was done by inverting the experimental VCO output and mapping the signal to a function that generates a linear frequency sweep. When applying this corrected voltage ramp, mirror measurements yield a significantly flatter beat frequency, demonstrating the improved linearity of the frequency sweep. The effect can be observed on the bottom part of figure 5, along with the shape of the requested voltage ramp. This calibration procedure is essential to ensure a proportional relation between beat frequency and group delay, to achieve reliable electron density profile measurements with the microwave reflectometer.

3.2. Signal filtering

Figure 1(b) shows that the bistatic antennas of the reflectometer are located between and behind the copper straps of the ICRH antenna. In vacuum, the expected main component of the reflection must come from the back wall of the machine, but the metallic environment, combined with the proximity of large 3D shaped conducting structures, provides multiple potential reflecting surfaces in addition to the wall. As a result, the probing microwave signal can experience several reflections before reaching the receiving horn, leading to complex signals.

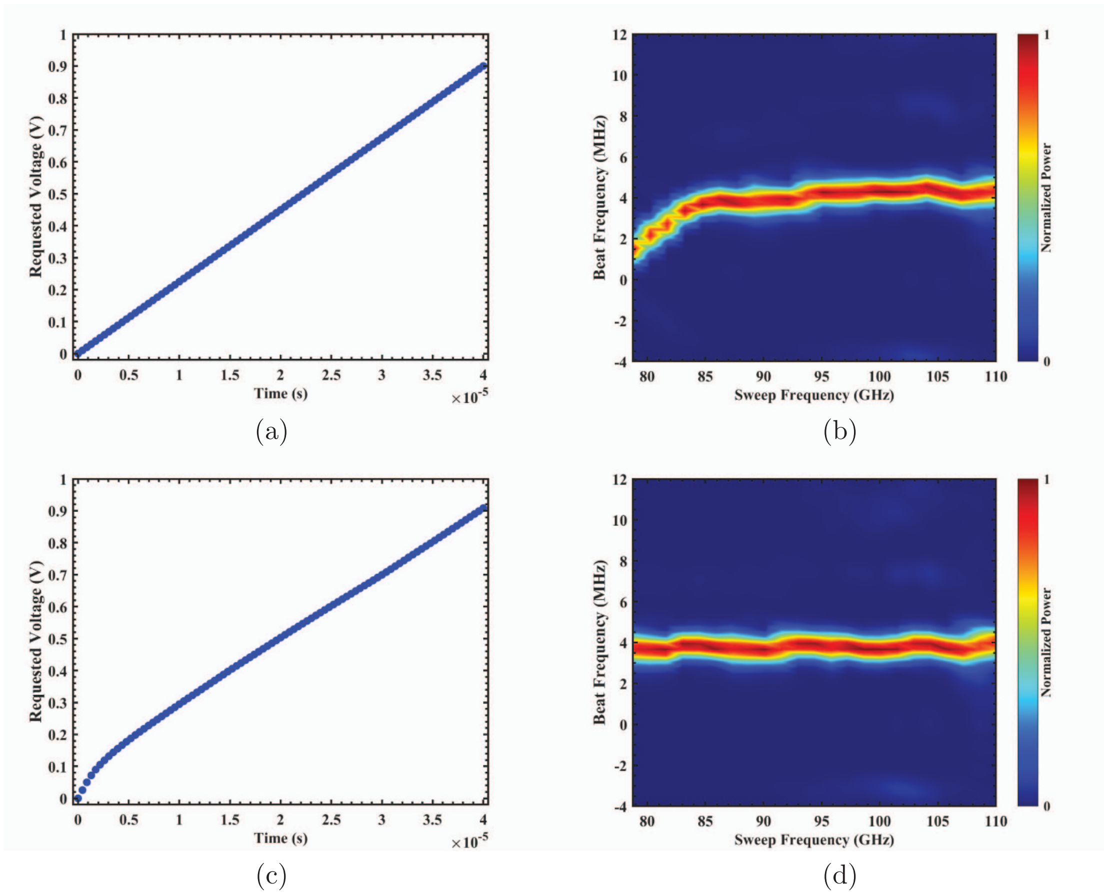

Figure 5. (a) Linear voltage ramp from the arbitrary waveform generator and (b) the measured beat frequency from a metallic mirror fixed at a constant distance. (c) Modified voltage ramp from the experimental VCO response and (d) the improved constant beat frequency from a metallic mirror fixed at a constant distance. The color scale indicates the power of the beat frequency.

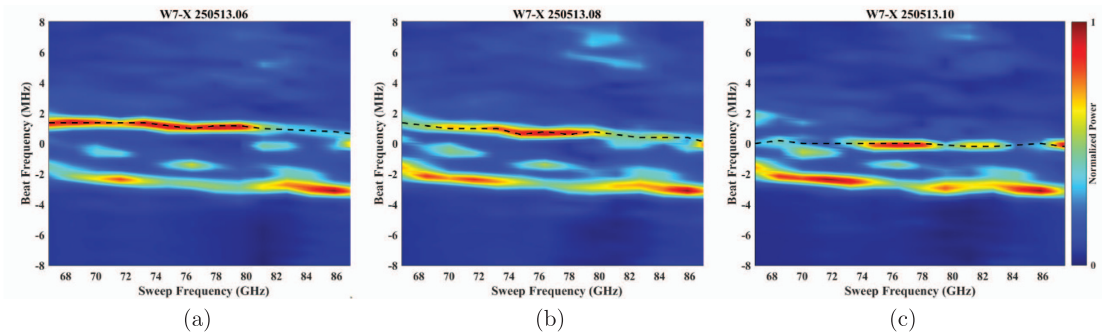

Figure 6. Measured beat frequency in vacuum averaged over 10 voltage ramps. The radial position of the ICRH antenna was changed to show the modification on the signal reflected on the back wall of the machine. The three plots show the results for the antenna positions with respect to the low field side wall: (a) −90 mm, (b) 0 mm, and (c) +200 mm. The dotted black line shows the beat frequency component used for the density calculation. The color scale indicates the power of the beat frequency.

Figure 6 shows examples of spectrograms from the microwave reflectometer in W7-X in vacuum. The multireflection effect is evident in these vacuum measurements, the spectrograms of the beat frequency exhibit several distinct branches instead of a single dominant component. These branches correspond to different effective propagation delays and indicate the presence of multiple reflections within the antenna box and surrounding structures.

When the data presents additional components distant from the dominant reflection, like the antenna parasitic cross talk, they can be suppressed by using band-pass filters [28]. However, when the additional frequency components are very close to the signal of interest, using filters can result in cutting out the useful signal and degrade the quality of the density profile estimations.

To identify the origin of the reflections present in figure 6, a distance scan was performed by mechanically translating the entire ICRH antenna trolley radially, changing the distance between the reflectometer horn antennas and the back wall of the stellarator. From the equation (2), it can be seen that, by keeping the frequency sweep rate constant and changing the radial position of the antenna, the beat frequency branch corresponding to the back wall reflection must change due to the modification of the length of the wave path and the group delay time. This test has already been performed during the commissioning phase to prove the correct behavior of the reflectometer [20].

Figure 6 shows that the top branch of the spectrogram changes when the antenna trolley is moved radially (a) −90 mm, (b) 0 mm, and (c) +200 mm with respect to the low field side wall. Equation (2) can be used to calculate the change of the beat frequency as a function of the change in the antenna position, by substituting the delay time τ_g for the time it takes the waves to cover twice the distance d between the horn antenna and the back wall:

$$\Delta f_{\text{beat}} = \left(\frac{2}{c}\right)\frac{\mathrm{d}f}{\mathrm{d}t}\Delta d. \tag{3}$$

In figure 6, the beat frequency changes from approximately 1.45 MHz to 1 MHz to 0 MHz, according to the change in distance between the horn antennas of the reflectometer and the back wall. Using equation (3), it can be calculated that a change of 90 mm in the position of the horn antenna generates a change of 0.45 MHz in the beat frequency, and a change of 200 mm produces a variation of exactly 1 MHz in the beat frequency. The estimations match the results presented in figure 6 for the variation of the top branch of the beat frequency as a function of the position of the antenna.

The bottom branch of the beat frequency, present in the results of figure 6, does not change during the distance scan. The bottom component can be observed at −2.3 MHz and remains constant during the position scan. This means that the reflection originating from the back wall exhibits a clear and predictable variation of the beat frequency with distance, while internal reflections remain insensitive to this displacement. This test allows the discrimination between reflections associated with the external reference surface and those generated within the antenna structure itself.

To mitigate the impact of multireflections on the density profile reconstruction, the spectrograms are processed using selective moving filtering techniques designed to track the top branch of the beat frequency and remove the unwanted components associated with other reflections, by changing the filter frequency limits as a function of the probing frequency. The dotted black line in figure 6 follows the branch of the beat frequency used for the density profile estimations. This filtering process is essential to ensure that only the appropriate signal is used in the calculation of the group delay and in the determination of the electron density profile.

4. Electron density profiles

The electron density profiles are obtained by inverting the phase variation according to the Bottollier-Curtet inversion algorithm [29], a standard method for FMCW reflectometry used in several fusion devices [30–32]. This technique uses FFTs to determine the beat frequency spectrum from the spectrogram and reconstruct the plasma permittivity profile from the measured group delay. For X-mode propagation, the refractive index depends on both the local electron density and the magnetic field, and the cutoff condition is given by the X-mode dispersion relation. Using the known magnetic field profile of W7-X, obtained using the MAG3D Biot–Savart code [23], the cutoff positions are mapped to electron density values, estimating the density profile in the plasma edge.

Following equation (1), the first cutoff is obtained when the density is zero and $\omega_1 = \omega_{ce}$. Using the magnetic field profile, this condition determines the initial radial position of the density profile, allowing to start the Bottollier-Curtet process. This position is defined as the zero-density point, in other machines the first cutoff can be observed experimentally by sweeping the probing frequency and finding a sudden change in the beat frequency and a large increase of the amplitude of the signal, which means a reflection in the plasma [12, 30]. Applying equation (1) to the standard magnetic field configuration in W7-X shows that the first reflection at the edge should occur at a probing frequency of approximately 64 GHz. However, the minimum probing frequency generated by the E-band system is 67.2 GHz, so the change in beat frequency and amplitude is not visible.

To solve this problem, an algorithm has been implemented [17] since OP2.1. The procedure uses the edge density profiles measured by the Alkali beam emission spectroscopy (ABES) technique [33] and traces the field lines from the toroidal position of the ABES diagnostic to the position of the microwave reflectometer, in order to map the density profile to the LOS of the reflectometer. The algorithm uses the

W7-X field line tracer code [34] and has shown a strong agreement between the edge density profiles calculated by both diagnostics [17]. This process has been used to find the zero-density point used in the construction of the electron density profiles in this paper. A new VCO is currently being tested and installed for the upcoming experimental campaign, the goal is to be able to sweep the probing frequency from values below the first cutoff in the standard field configuration, to directly find the change in the beat frequency related to the zero-density point and improve the accuracy of the calculated edge density profiles.

4.1. Comparison of the edge density profiles

The validation of the reconstructed electron density profiles is essential to assess the reliability of the reflectometer measurements. For this purpose, the reflectometer results are compared with measurements from the Thomson scattering diagnostic, which provides independent electron density profiles [35]. The toroidal positions of both diagnostics are relatively close, which allows the use of the field line tracer code [34] to map the density measurements to the LOS of the reflectometer. While the reflectometer primarily probes the plasma edge region and Thomson scattering measurements are mostly focused on the plasma core, there exists a small radial overlap region close to the LCFS where both diagnostics can be compared, especially in low density experiments when the reflectometer can measure a wider region reaching the LCFS. The density data points from the Thomson scattering diagnostic inside the LCFS are compared with the reflectometer data expressed in the effective radius r_{eff}. A locally weighted scatterplot smoothing (Lowess) fit has been applied to the Thomson scattering data inside the LCFS. In the edge region outside of the LCFS, the reflectometer data is compared to the density profiles provided by the ABES system [33]. This comparison is more qualitative because the density is not necessarily constant along the field lines, but the ABES profiles can be mapped to the toroidal position of the reflectometer using the EXTENDER code [36] for the VMEC equilibrium in the standard magnetic field configuration.

A direct comparison between the electron density profiles obtained from X-mode reflectometry, ABES, and Thomson scattering is presented in figure 7. Figure 7(a) presents the time traces of the electron cyclotron resonance heating (ECRH) and ICRH injected power, along with the line integrated density calculated automatically by the dispersion interferometer [37] for the hydrogen discharge 20250515.046. The vertical dotted lines in the time traces show the time instants selected for the calculation of the electron density profiles. In this shot, the injected ICRH power was approximately 0.45 MW at 25 MHz.

The bottom two plots (b) and (c) of figure 7 show the results obtained with the Thomson scattering system, ABES, and the microwave reflectometer. The Thomson scattering data is presented only inside the LCFS and the ABES data is compared to the density profile measured by the reflectometer only on the region outside the LCFS, where the ABES diagnostic is more reliable. For this comparison, the ABES density profile from shot 20250515.056 was used because it provides a data set for the same density and magnetic field configuration as the shot presented in figure 7(a). The edge density profiles estimated by the reflectometer show good agreement with both density profile diagnostics within experimental uncertainties, providing confidence in the accuracy of the beat frequency calibration, signal processing, and density inversion procedure. This validation demonstrates the capability of the reflectometer to reliably measure edge electron density profiles in the vicinity of the ICRH antenna and to complement core diagnostics in the overall characterization of the plasma density distribution.

The time instants for the plots (b) and (c) of figure 7 are selected to compare the density profiles before and during the ICRH antenna operation. Both measured edge and core density profiles show a very similar behavior during the two instants, which shows that the presence of RF power from the ICRH antenna does not disturb the measurements of the microwave reflectometer. In simulations [38] and experiments in other machines [39], it was observed that the variations of the electric field generated by the straps caused radial particle flows towards and away from the antenna due to the ponderomotive force. The first results do not show any modification of the low density in the region in front of the antenna, more experiments are required to study this effect in detail.

Figure 8 presents the results of the reflectometer measurements during an experiment designed to ramp up the density in the hydrogen discharge 20250522.059. Figure 8(a) shows the time traces of the ECRH power and the line integrated density in the machine. The vertical dotted lines show the time instants used for the calculation of the electron density profiles and have been selected to emphasize the changes of the measurements as a function of the total density in the machine.

The time instants are selected at $t = 8$ s, when the line integrated density is $5.0 \times 10^{19}\,\mathrm{m}^{-2}$; $t =$ 14 s, when the line integrated density is $10 \times 10^{19}\,\mathrm{m}^{-2}$; and $t = 20$ s, when the line integrated density

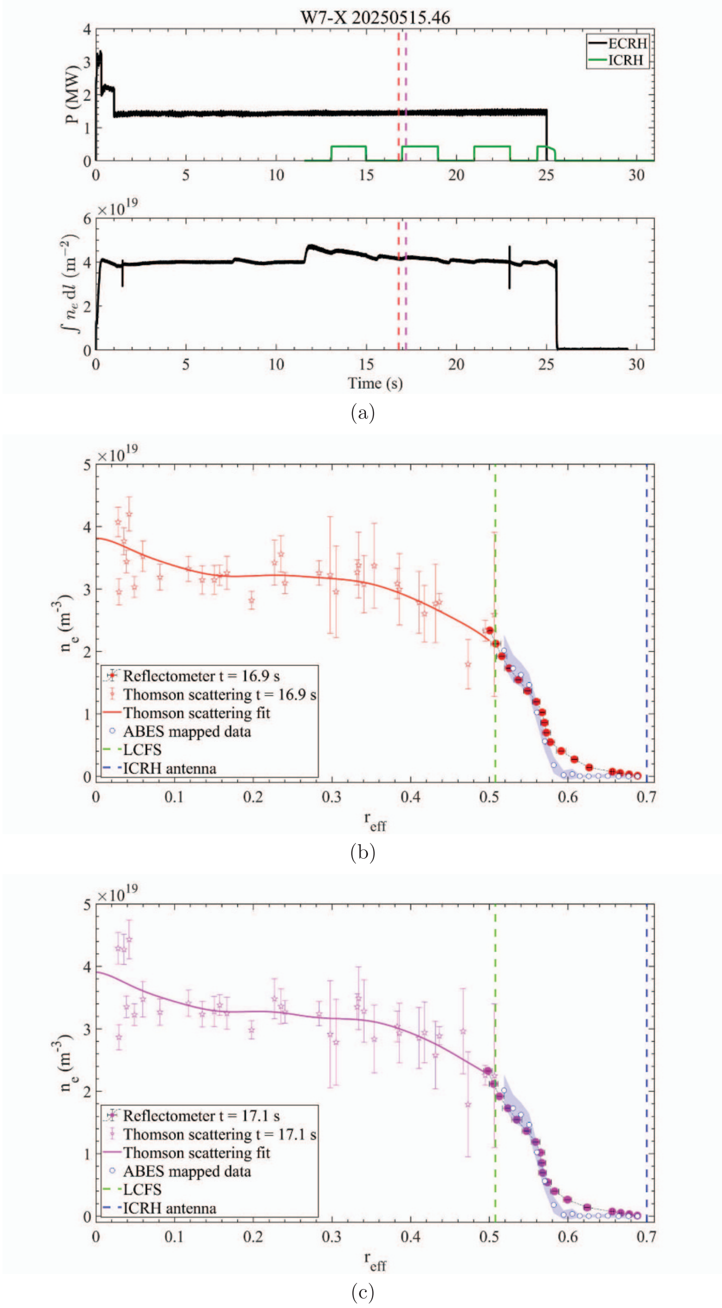

Figure 7. (a) Time traces for shot 20 250 515.46 in W7–X. The top part shows the injected ECRH and ICRH power and the bottom part shows the line integrated density during the experiment. The vertical dotted lines show the time instants selected for the calculation of (b) and (c). (b) Experimental electron density profile calculated at $t = 16.9$ s with Thomson scattering, ABES, and the edge density profile reflectometer. The time instant is selected before the ICRH pulse. (c) Experimental electron density profile calculated at $t = 17.1$ s with Thomson scattering, ABES, and the edge density profile reflectometer. The time instant is selected during the ICRH pulse.

increases to $14 \times 10^{19}\,\mathrm{m}^{-2}$. Figure 8(b) shows the density profile calculation with both Thomson scattering and microwave reflectometry during those time stamps. There is a clear increase of the core density measured by the Thomson scattering system, as expected, and the edge density profiles estimated by the reflectometer reflect this global increase of the density. Due to the range of the frequency sweep using E-band, the maximum density of the edge profile reflectometer is limited to $n_e = 2.0 \times 10^{19}\,\mathrm{m}^{-3}$. When the global density is higher, this value is closer to the edge region, limiting the probing distance of the reflectometer. Figure 8(c) presents a zoomed in version of the previous plot, to highlight the changes in the edge density profiles during the density ramp up. The reflectometer data can be used to find the position of the rapid increase in density outside the LCFS, this information is useful to define the safe

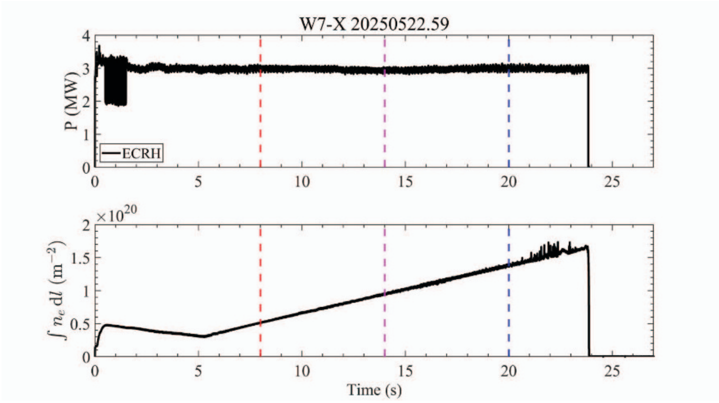

(a)

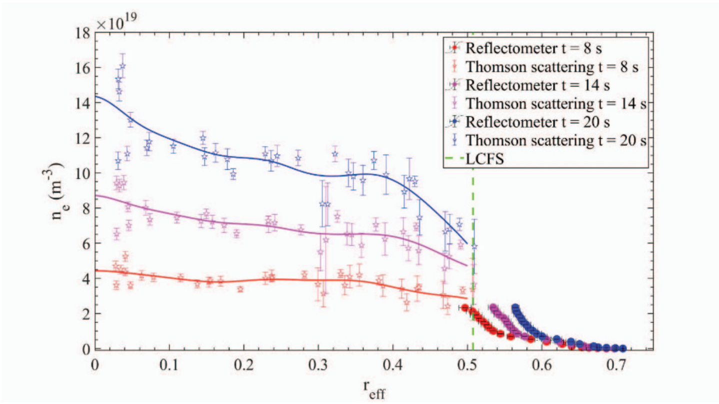

(b)

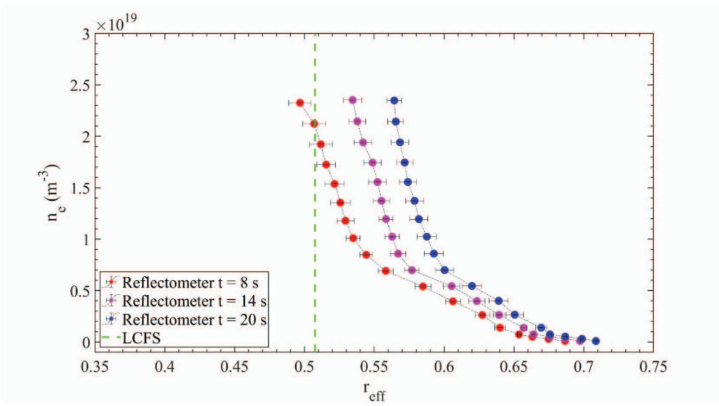

(c)

Figure 8. (a) Time traces for shot 20 250 522.59 in W7-X. The top part shows the injected ECRH power and the bottom part shows the line integrated density, ramped linearly during the experiment. The vertical dotted lines show the time instants selected for the calculation of the density profiles. (b) Experimental electron density profiles calculated at three different time instants with Thomson scattering and the edge density profile reflectometer. (c) Zoomed in version of the reflectometer data from (b) to highlight the changes of the density outside the LCFS.

radial region for the movable ICRH antenna system. The results show the edge density profiles measured with the microwave reflectometer are in qualitative agreement with both the Thomson scattering density profile measurements and the dispersion interferometer line integrated densities. The results confirm additional reports of the change on the edge profiles as a function of the global density in W7-X [20, 40].

5. Conclusions

A microwave reflectometer has been installed and commissioned at the ICRH antenna on Wendelstein 7-X to measure the electron density profiles in the plasma edge region. The diagnostic has been tested in both vacuum and plasma conditions, and stable operation has been demonstrated during experimental campaigns. Calibration procedures, including correction of the frequency sweep linearity and selective filtering of the beat frequency spectrograms, were developed to improve the collected signals and estimated density profiles. Although microwave reflectometry has been widely used on many fusion devices, the present implementation is unique because the diagnostic is directly integrated inside the movable ICRH antenna structure, this demonstrates the feasibility of operating a reflectometer in a stellarator environment, within a complex metallic structure and in close proximity to the copper straps of the antenna, and represents an important step toward reliable edge diagnostics in reactor-relevant conditions.

The electron density profiles obtained for hydrogen plasmas in the standard magnetic field configuration on W7-X show strong agreement with Thomson scattering measurements inside the LCFS, and ABES in the region outside the LCFS, as shown in figure 7. The validation improves the confidence in the signal processing, calibration, and density inversion methods employed during the operational phase OP2.3, and confirms the capability of the reflectometer to reliably resolve edge density profiles in front of the ICRH antenna. Furthermore, the measured edge density profiles respond as expected to changes in the global plasma density, with a clear increase in edge density observed during density ramp-up experiments, as shown in figure 8.

From the perspective of the ICRH system, the availability of accurate edge density profiles in front of the antenna is essential. The plasma density in this region strongly influences the wave coupling efficiency between the antenna and the plasma, direct measurements of the SOL density provide critical input for improving coupling calculations. Most importantly, a reflectometer at the position of the ICRH antenna avoids the complexities and inaccuracies involved in the mapping of the density profiles that are measured in the edge region at another toroidal angle of the stellarator.

The results demonstrate that the microwave reflectometer is operational together with the ICRH system, but indicate that the RF waves do not strongly perturb the local edge density in front of the antenna. More ICRH experiments are necessary to study fast particle confinement, ion cyclotron wall conditioning, and plasma heating. The microwave reflectometer will be used to study in more detail the density profiles in front of the ICRH antenna during those experiments. The measured edge density profiles are directly relevant for operational considerations of the ICRH system. The data can be used to define safe operating conditions for the radially movable antenna trolley. In particular, the density measurements contribute to determining a safe distance between the antenna and the plasma, ensuring both efficient coupling and protection of the antenna components from excessive heat loads or plasma interactions. In future tests, the edge density profile reflectometer will be a valuable tool to understand the behavior of the plasma in front of the ICRH antenna and provide information to improve the performance and safe operation of the heating system and the measured electron density profiles could also be used as input for simulations of the RF waves in the complex 3D geometry of W7-X [41].

Acknowledgments

This work has been carried out within the framework of the EUROfusion Consortium, funded by the European Union via the Euratom Research and Training Programme (Grant Agreement No 101052200–EUROfusion). Views and opinions expressed are however those of the authors only and do not necessarily reflect those of the European Union or the European Commission. Neither the European Union nor the European Commission can be held responsible for them.

Data availability statement

All data that support the findings of this study are included within the article (and any supplementary files).

ORCID iDs

D López-Rodrıguez 0000-0001-5246-4972
A Krämer-Flecken 0000-0003-4146-5085
H M Xiang 0000-0001-7799-6190
X Han 0000-0001-8498-6433
K Crombé 0000-0001-9883-3972
J Ongena 0000-0001-7456-4739

D A Castaño-Bardawil 0000-0003-2125-8310
A Adriaens 0009-0002-0200-8375
M Verstraeten 0000-0002-6972-7625
D Hartmann 0000-0002-3511-6500
M Vergote 0000-0003-2148-6903

References

[1] Warmer F *et al* 2015 *Fusion Eng. Des.* **91** 60–66
[2] Endler M *et al* 2021 *Fusion Eng. Des.* **167** 112381
[3] Grulke O *et al* 2024 *Nucl. Fusion* **64** 112002
[4] Klinger T *et al* 2017 *Plasma Phys. Control. Fusion* **59** 014018
[5] Lazerson S *et al* 2024 *Phys. Plasmas* **31** 072506
[6] Ongena J *et al* 2023 *Fusion Eng. Des.* **192** 113627
[7] Slaby C *et al* 2025 *Plasma Phys. Control. Fusion* **67** 065041
[8] Lerche E *et al* 2011 *Plasma Phys. Control. Fusion* **53** 124019
[9] Sirinelli A *et al* 2010 *Rev. Sci. Instrum.* **81** 10D939
[10] Clairet F *et al* 2010 *Rev. Sci. Instrum.* **81** 10D903
[11] Zeng L *et al* 2006 *Nucl. Fusion* **46** S677–84
[12] Wang Y M *et al* 2013 *Fusion Eng. Des.* **88** 2950–5
[13] Hirsch M, Holzhauer E and Hartfuss H-J 2006 *Nucl. Fusion* **46** S853–61
[14] Yokota Y *et al* 2008 *Rev. Sci. Instrum.* **79** 056106
[15] Han X *et al* 2025 *Fusion Sci. Technol.* **67** 045011
[16] Han X *et al* 2023 *14th Int. Reflectometry Workshop*
[17] Xiang H M *et al* 2023 *49th EPS Conf. on Plasma Physics* vol P2.015
[18] Aguiam D E *et al* 2016 *Rev. Sci. Instrum.* **87** 11E722
[19] Jamann A *et al* 2025 *Plasma Phys. Control. Fusion* **67** 085036
[20] Xiang H M *et al* 2026 *Plasma Sci. Technol.* **28** 035601
[21] Mazzucato E 1998 *Rev. Sci. Instrum.* **69** 2201–17
[22] Hirshman S P and Whitson J C 1983 *Phys. Fluids* **26** 3553–68
[23] Grahl M *et al* 2018 *IEEE Trans. Plasma Sci.* **46** 1114–9
[24] Lore J D *et al* 2019 *Nucl. Fusion* **59** 066041
[25] Ongena J *et al* 2014 *Phys. Plasmas* **21** 061514
[26] Sabot R *et al* 2006 *AIP Conf. Proc.* 812
[27] Zhang S *et al* 2014 *Plasma Sci. Technol.* **16** 311–5
[28] Shelukhin D A *et al* 2018 *Rev. Sci. Instrum.* **89** 094708
[29] Bottollier-Curtet H and Ichtchenko G 1987 *Rev. Sci. Instrum.* **58** 539–46
[30] Clairet F *et al* 2001 *Rev. Sci. Instrum.* **72** 340–3
[31] Zhong W L *et al* 2005 *Rev. Sci. Instrum.* **85** 013507
[32] Subramaniyan N *et al* 2026 *NDT E Int.* **158** 103558
[33] Vécsei M *et al* 2021 *Rev. Sci. Instrum.* **92** 113501
[34] Bozhenkov S A *et al* 2013 *Fusion Eng. Des.* **88** 2997–3006
[35] Pasch E *et al* 2016 *Rev. Sci. Instrum.* **87** 11E729
[36] Drevlak M, Monticello D and Reiman A 2005 *Nucl. Fusion* **45** 731–40
[37] Brunner K J *et al* 2018 *J. Instrum.* **13** P09002
[38] Van Eester D and Crombé K 2015 *Phys. Plasmas* **22**
[39] Koch R *et al* 2005 *Fusion Sci. Technol.* **47** 97–107
[40] Krämer-Flecken A *et al* 2025 *J. Instrum.* **20** C12008
[41] Slaby C *et al* 2026 *EPJ Web Conf.* **346** 02006